Modelling the sequential earthquake-tsunami response of coastal urban transport infrastructure

Azucena Román-de la Sancha[1], Rodolfo Silva[2], Omar S. Areu-Rangel[1], Manuel Gerardo Verduzco-Zapata[3], Edgar Mendoza[2], Norma Patricia López-Acosta[2], Alexandra Ossa[2], Silvia García[2]

1 Graduate student, Instituto de Ingeniería, Universidad Nacional Autónoma de México, Circuito Escolar, Ciudad Universitaria, 04510, Coyoacán, Cd. Mx., México

2 Researcher, Instituto de Ingeniería, Universidad Nacional Autónoma de México, Circuito Escolar, Ciudad Universitaria, 04510, Coyoacán, Cd. Mx., México

3 Researcher, Facultad de Ciencias Marinas, Universidad de Colima, Carretera Manzanillo-Cihuatlán Km 19.5, Colonia El Naranjo. 28868 Manzanillo, Colima, México

Correspondence to: Azucena Román-de la Sancha (azucena.roman@ingenieria.unam.edu)

Abstract. Transport networks in coastal, urban areas are extremely vulnerable to seismic events, with damage likely due to both ground motions and tsunami loading. Most existing models analyse the performance of structures under either earthquakes or tsunamis, as isolated events. This paper presents a numerical approach that captures the sequential earthquake-tsunami effects on transport infrastructure in a coastal area, taking into consideration the combined strains of the two events. Firstly, the dynamic cyclical loading is modelled, applied to the soil-structure system using a finite difference approximation to determine the differential settlement, lateral displacement, and liquefaction potential of the foundation. Next, using a finite volume method approach, tsunami wave propagation and flooding potential are modelled. Finally, the hydrostatic and hydrodynamic loads corresponding to the wave elevation are applied to the post-earthquake state of the structure, to obtain a second state of deformation. The sequential model is applied to an embankment in Manzanillo, Mexico, which is part of a main urban road, the response is analysed using ground motion records of the 1995 Manzanillo earthquake-tsunami event.

1. Introduction

Transportation networks are key elements of the economy and society; therefore, more attention has been paid to the need for sustainable, adaptive and resilient transport systems under natural hazards and other emergency conditions in the last decades. Past experience of the subduction mechanisms of seismic events has shown the vulnerability of transport infrastructure located in coastal urban areas associated with the cascade effect of earthquake-tsunami-flooding-ground motion (Bhattacharya et al., 2017; Koshimura et al., 2014; Rowell and Goodchild, 2017; Sarkis et al., 2018; Williams et al., 2020). Existing methodologies to analyse the response of transport assets during earthquake and tsunami conditions consider these phenomena as independent events. Probabilistic analyses and fragility curves (Akiyama et al., 2020; Burns Patrick et al., 2021) are examples of multi-hazard approaches that aim to determine the occurrence probability of both phenomena simultaneously and the expected level of damage of structures after them. Recent multi-hazard literature has focused on structures in the urban environment such as buildings and bridges (Attary et al., 2021; Burns Patrick et al., 2021;

Ishibashi et al., 2021; Karafagka et al., 2018), while little attention has been paid to the response of road

35   networks to sequential earthquake-tsunami processes (Iai, 2019).

The impacts of a combined earthquake-tsunami on urban transport networks have important economic and social effects in the short, medium and long terms, in both human and material losses. These impacts are fundamentally associated with the loss of connectivity of regions or cities, which primarily disturb the continuity of rescue efforts, reconstruction, urban logistics, health and safety activities (Dizhur et al., 2019;

40   Sarkis et al., 2018). Most of the negative effects are associated with partial or total damage to urban and interurban roads that disrupt land communication between key sites (Cubrinovski, 2013). In coastal areas, one significant factor causing damage in earthquakes is the increase in the pressure within the soil mass induced by the seismic loads, and by the accumulation of hydrodynamic pressure in the non-cohesive saturated soils common in these areas. From observations of past events in coastal areas it is seen that moderate seismic

45   intensity can cause liquefaction, resulting in reduced stiffness and a loss of shear strength in liquefied soils. This can lead to soil settlement, increased lateral ground pressure, and loss of strength (Kakderi and Pitilakis, 2014), bringing about damage to structures, sometimes even causing their collapse, and in the case of embankments, potential slope-stability problems, or even landslides.

Regarding tsunami damage, one of the most critical aspects to consider is the hydrodynamic behaviour of the

50   wave as it approaches the coast. However, information on the physical parameters that characterize these waves is often limited, due to difficulties in achieving accurate measurements during the event.

The impact of a tsunami on the coast is governed by non-linear physics, such as turbulence (Klapp et al., 2020). The hydrodynamic behaviour during a tsunami is complex and can significantly affect structures. Forces induced by the hydrodynamics associated with a tsunami are governed by various fluid parameters, such as

55   density, velocity, and depth, as well as the geometry of the structure. These forces induced by the pressures and velocities of tsunamis are particularly important in the stability of coastal structures, affecting assets such as piers, embankments and bridge piles (Chinnarasri et al., 2013). Numerical approaches based on finite element methods (Argyroudis and Kaynia, 2015; Mckenna et al., 2021) and finite differences (Mayoral et al., 2016; Mayoral et al., 2017) have been applied to assess the seismic vulnerability and potential damage of transport

60   infrastructure. Likewise, the effects of hydrodynamic loads on structures have been estimated through modelling methods, such as finite volume method (Jose et al., 2017) and smooth particle hydrodynamic method (Altomare et al., 2015; Klapp et al., 2020).

Besides the simulation models available to assess the individual effects of earthquake and tsunami loads on transport infrastructure, a few, limited, modelling approaches to predict sequential damage and effects are

65   available. From a review of the literature on fragility and vulnerability models it was seen that most studies focus on individual transport components or networks, usually considering only one hazard at a time (Argyroudis and Kaynia, 2015; Argyroudis and Mitoulis, 2021; Briaud and Maddah, 2016; Iai, 2019; Maruyama et al., 2010; Nibs, 2004). The studies mentioned focus mainly on the vulnerability of bridges and tunnels, and the main emphasis is on ground movement due to seismic excitation. Research based on simplified models has

70   examined other structures such as embankments, slopes, retaining walls, and abutments. Existing models for

these elements are based on empirical data or expert judgment, mainly for seismic analysis, and focus on a universe of limited typologies.

There is, at present, the opportunity to improve the modelling approaches that consider more structure types, as well as multiple hazards, including earthquakes and tsunamis simultaneously. To extend these studies, the risk analysis can be extended by using one of the methodologies described by (Escudero Castillo et al., 2012) or better yet, by implementing an analytical framework similar to the Drivers-Exchanges-State of the environment-Consequences-Responses (DESCR) framework proposed by (Escudero Castillo et al., 2012; Silva et al., 2020) in which ecosystem-based adaptation and community-based adaptation is considered (Silva et al., 2019).

This paper proposes a numerical approach to capture the sequential earthquake-tsunami effects on urban road embankments located in coastal areas. The approach allows the effective stress paths and corresponding soil strain evolution during the event to be considered, taking into account soil-embankment response, tsunami propagation, and hydrodynamic behaviour. The first step consists of computing the initial static stress and deformation conditions, and modelling the dynamic cyclic loading applied to the soil-embankment system in an earthquake. A finite difference approximation is used to determine the differential settlements and lateral displacements, associated with excess pore pressure generation during cyclic loading. This allows the assessment of the liquefaction potential of the soil foundation. Next, a finite volume approach and smooth particle hydrodynamics are combined, to model tsunami wave propagation at oceanic level and flooding potential. Finally, the resulting sea-surface elevation and hydrodynamic loads are applied to the post-earthquake state of the structure to obtain the final deformation state.

2. Sequential earthquake-tsunami response model on transport infrastructure

The sequential model proposed is comprised of three steps, Figure 1. The first step is the numerical analysis of the seismic response of the soil-structure system. The next stage corresponds to the wave generation and propagation model from deep, offshore waters up to the coast. Finally, there is the analysis of the soil-structure system response to hydrodynamic loadings, given the state of deformation induced by the seismic excitation. This methodology is applied to an embankment of urban road, in the coastal city of Manzanillo, Mexico.
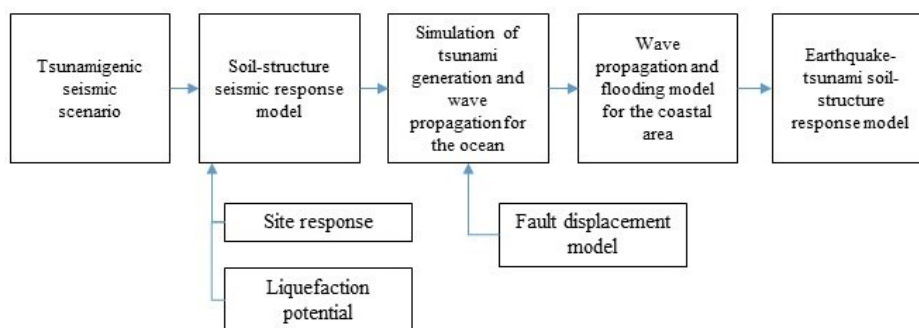
Figure 1: Evaluation of the sequential earthquake-tsunami effects on transportation infrastructure.

3. Case study

Manzanillo, on the Mexican Pacific Coast, is the most important commercial port in the country. The zone is
seismically complex, due to the triple junction of the Cocos and Rivera subduction plates that are moving
towards and below the continent, on the North American Plate, Figure 2. The city has been affected by many
major earthquakes, and several in the last century (Tonatiuh Dominguez et al., 2017; Eqe International, 1996;
Ovando-Shelley and Romo, 2004). In 1995, an earthquake Mw = 8 caused significant damage, mainly in the
coastal area of the city, where collapsed buildings were reported and liquefaction of the saturated sandy soils
was observed at several locations in the port area of Manzanillo.
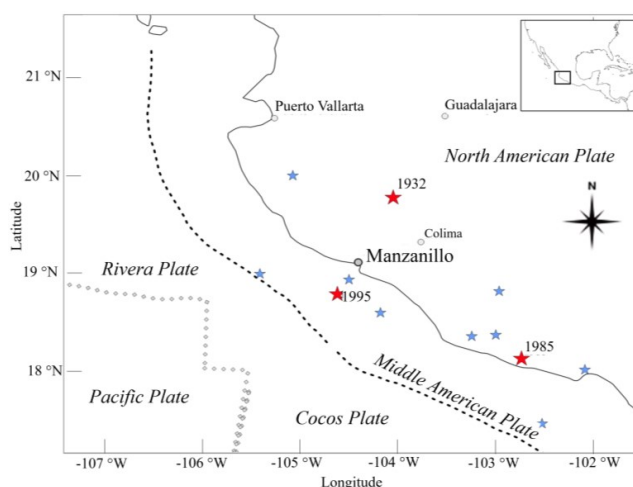
Figure 2: Seismic environment of the study area. Red stars indicate earthquakes M ≥ 8.0, blue stars indicate earthquakes 7.0 ≤ M ≤ 8.0.

The urban area of Manzanillo and its commercial port are connected to the rest of Mexico via the Colima-
Manzanillo, Manzanillo-Puerto Vallarta and Cuyutlán-Manzanillo highways. Part of the embankment on one
of these main avenues was selected for the analyses performed in this research. The Boulevard Miguel de la
Madrid, runs parallel to Miramar Beach, which is on Santiago Bay, NW of the city of Manzanillo, Figure 4.
This beach has attractive natural characteristics, perfect for practicing sun and beach recreation activities
(Cervantes et al., 2015); the road has become a waterfront promenade, with several restaurants and access points
to the beach along the road. This road also connects the communities of El Naranjo, in the west, and Colinas de
Santiago, in the east. It is also an important public transport route, serving tourists and the labour force going
to and from the restaurants, hotels and recreation facilities. Further west is Manzanillo International Airport.
This road is therefore a vital part of the infrastructure of the city, facilitating many social-economic activities.

Figure 3: Aerial views of Boulevard Miguel de la Madrid.

120

The data on the topography and topology of the section of embankment analysed here were obtained in field work carried out in 2021. A total of 24 topographic profiles along a 2 km long section were surveyed, Figure 4. The surveying equipment eSurvey E300 PRO + P8II GNSS was positioned at a control point to later link the collected data with the official datum. With a centimeter precision, post-processing of the data gave the

125   coordinates of a geodesic point which served as a reference to carry out the topographic survey. Based on the geometric characteristics of these cross-sections and their relative importance, the cross-section shown in Figure 5 was selected for the sequential earthquake-tsunami analysis.
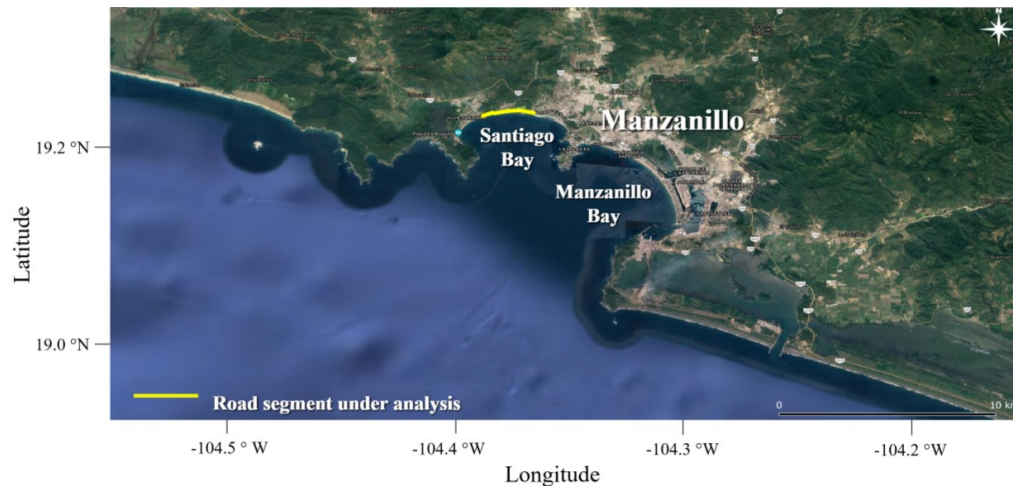
130   **Figure 4. Location of the road embankment analysed (© Google Earth).**
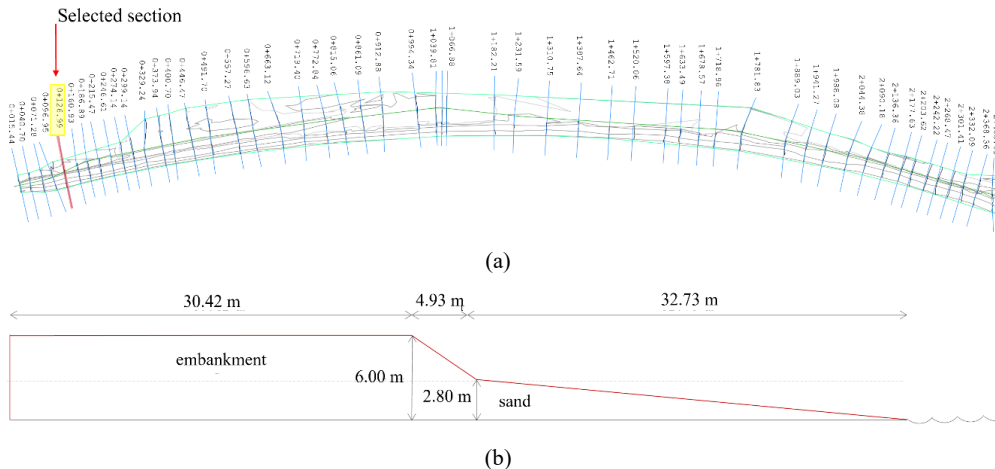
Figure 5: (a) Cross sections taken along the road and (b) the cross-section used in the analysis.

3.1. Seismic and geotechnical characterization of the study area

Manzanillo is in the northern part of the Sierra Madre del Sur mountain range. Geological studies by (Tonatiuh Dominguez et al., 2017) state that granite intrusions, extrusive igneous outcrops and limestone deposits are

135 found in the region. Deposits of clay and organic materials are also found in the two saltwater lagoons nearby. Sand deposits are found along the coast and alluvial deposits are found around the igneous deposits, Figure 6. Based on geophysical explorations at points S1 to S5, Figure 6, (Tonatiuh Dominguez et al., 2017) shows an in situ characterization of some dynamic properties, such as shear wave velocities. Figure 7 depicts the shear wave velocities obtained from exploration at Site 4, which is considered representative for characterizing sites with

140 soil type B, where the section of the road embankment studied is located.
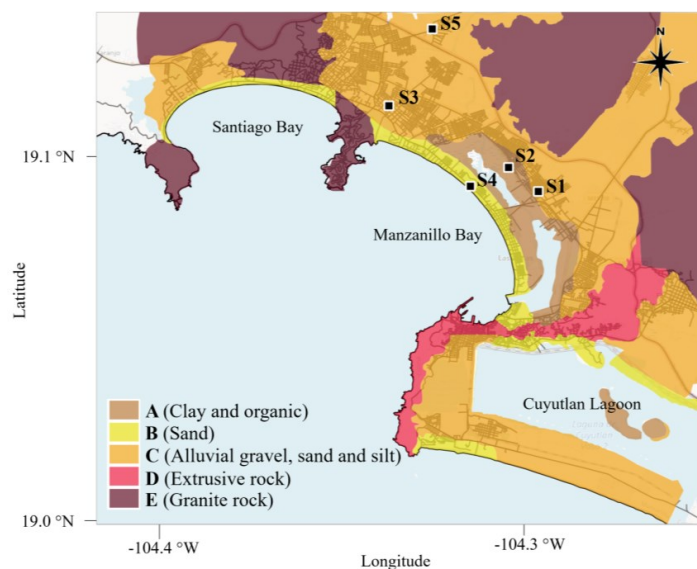
Figure 6: Survey sites S1 - S5 and geotechnical characterization of Manzanillo and Santiago Bays obtained from (Tonatiuh Dominguez et al., 2017).
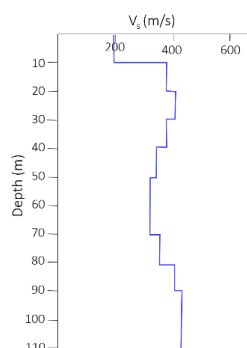
145 **Figure 7: Shear wave velocity at Site 4, according to (Tonatiuh Dominguez et al., 2017).**

Manzanillo is located in the subduction zone between the Rivera and Cocos tectonic plates with the North American plate. The rate of displacement at the contact surfaces is about 50 to 70 mm per year, (Demets and Wilson, 1997), so the probability of severe earthquakes is high. Furthermore, in subduction zones, there is a high likelihood of tsunami occurrence, given the vertical displacement generated on the seabed, which can be

150   several meters, extending over tens of thousands of square kilometers. Over time, numerous serious earthquakes have been recorded in this area, causing high intensity ground movements, both in the continental region and along the coastline, as well as tsunami damage on the coast. According to historical records, at specific sites in this area the wave heights associated with tsunamis have reached 10 m. Tsunamigenic events occurring in this region are of Mw>8 magnitudes, among which are the 1787, 1932, 1985 and 1995 earthquakes in the study

155   area.

3.2.   Tsunamigenic seismic scenario

The seismic features were characterized using records from the seismic station MZ01, Figure 8, located on sandy deposits. It is the only station in free-field conditions in Manzanillo that was operating during the 1995 event (Mw = 8.0). Table 1 summarizes the characteristics of the event. Figure 8 shows the location of station

160   MZ01 and the epicenter of the 1995 event. Figures 9 and 10 show the acceleration time histories and their corresponding response spectra for each parameter measured at station MZ01.

Table 1: Characteristics of the 1995 Manzanillo earthquake and the MZ01 station record.

Site	Event	Magnitude	Epicentral distance (km)	Soil	*PGA* (gal)
COLIMA (MZ01)	09/10/1995	M_w=8.0	47.5	Sand	N00E=380.25 V=187.58 N90E=402.9

Note: *PGA*: Peak ground acceleration
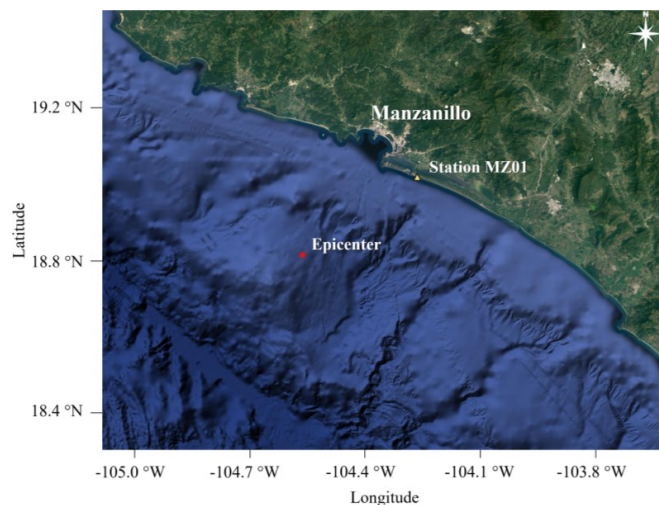
165   **Figure 8: Location of the seismic station MZ01 and the epicentre of the 1995 Manzanillo earthquake (Mw=8) event (© Google Earth).**
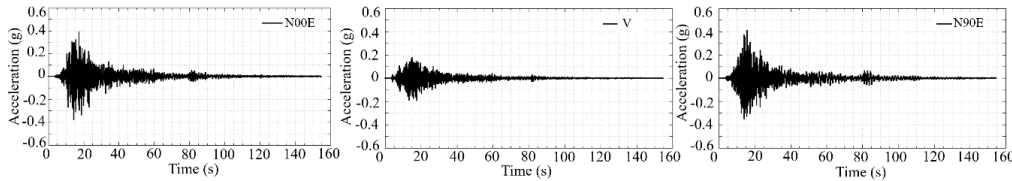
Figure 9: Acceleration time histories at station MZ01 during the 1995 Manzanillo earthquake (Mw=8.0) earthquake.
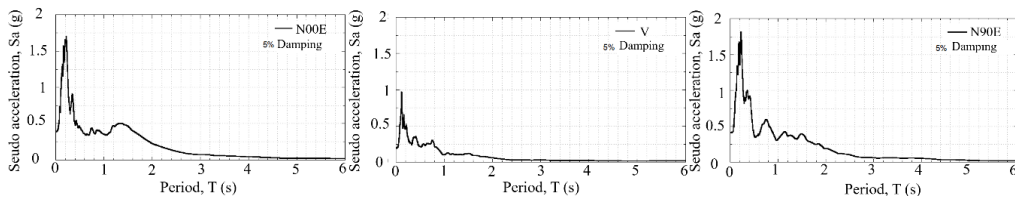
Figure 10: Response spectra from the time histories recorded at station MZ01 during the 1995 Manzanillo earthquake (Mw=8.0) earthquake.

To perform the analysis, the record of N90E component showing the larger accelerations and pseudo-accelerations was selected. The accelerations time history was baseline corrected to avoid residual velocities or displacements at the end of the movement, which could be confused with permanent displacements. Figures 11 (a) and (b) show the acceleration, velocity, and displacement histories before and after correction, respectively.
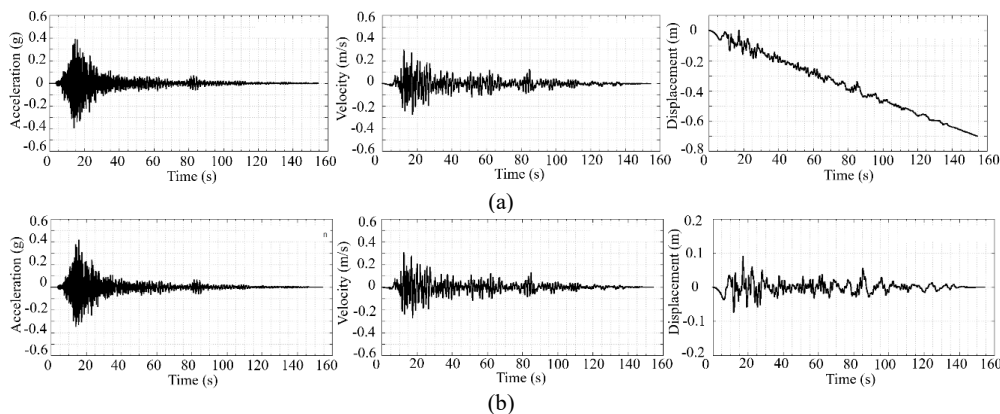
Figure 11: Acceleration, velocity and displacement time histories (a) without base line correction (b) with base line correction.

3.3. Step 1: seismic response

To simulate seismic wave propagation, during the earthquake, a site response analysis was performed using the N90E acceleration history. The record was deconvolved and propagated through the soil profile of the S4 site, performing a one-dimensional deterministic analysis. In this way, a first approximation of the expected dynamic amplification in the soil deposit was obtained, which is useful prior to the non-linear analysis in the time domain. This analysis also allows the maximum dynamic shear stresses in the soil to be obtained, which are used to

estimate the liquefaction potential in the simplified methods. Since dynamic laboratory tests were not performed on samples obtained near the study area, it was considered appropriate to assume the damping curves and shear stiffness modulus ratio presented by (Seed and Idriss, 1970) for sands, Figure 12.

(a)   (b)
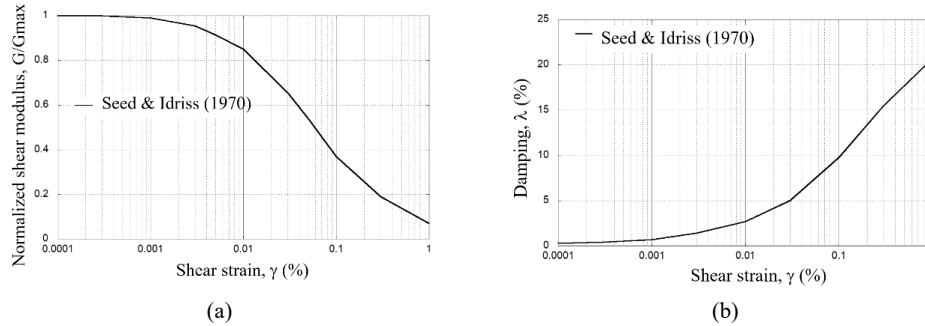
Figure 12: (a) Normalized shear stiffness curves G/G_{max} and (b) damping curves λ

190   The stress history was determined and transformed into an equivalent number of cycles of uniform shear stress. In this way, the intensity and duration of ground motions are considered, as well as the variations of shear stress with depth. For practical purposes, the equivalent number of cycles of shear stress, τav , can be estimated as 65% of the maximum stress, τmax (Seed and Idriss, 1970), Figure 13.

(a)   (b)
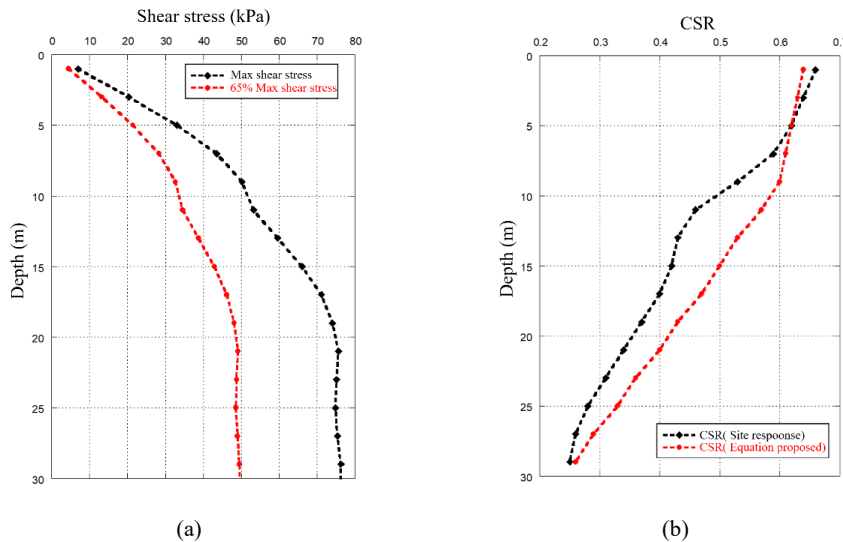
Figure 13: (a) Maximum shear stress profile for the study site, (b) cyclic stress ratio profile, using the equation
195   **proposed by Seed and Idriss (1971) and the site response analysis.**

The number of equivalent stress cycles *Neq* depends on the magnitude and duration of the earthquake. (Seed et al., 1975), applied a weighting procedure to establish a uniform number of cycles of shear stress *Neq* (with an amplitude of 65% of the maximum cyclic shear stress $\tau cyc = 0.65\tau max$) that would produce an equivalent pore pressure, where the number of cycles of uniform shear stress increases with increasing magnitude of the

200 earthquake. For the case study, an earthquake magnitude Mw = 8.0 corresponds to an equivalent number of

cycles of uniform shear stress equal to 21, Figure 14.
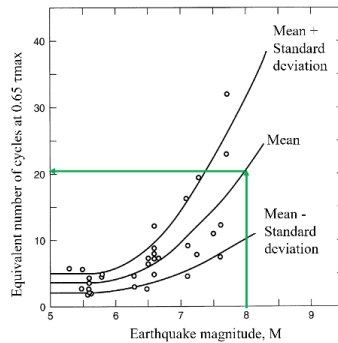
Figure 14: Equivalent number of uniform cyclic loading *Neq* for different seismic magnitudes (Martin et al. 1975)

205 The liquefaction potential of the soil was evaluated using the cyclic stress criterion (Kramer, 1996; Seed and

Idriss, 1970). One of the most common methods to evaluate liquefaction resistance is based on standard

penetration tests (SPT). This criterion uses the cyclical resistance ratio CRR from blow counts from the SPT

test, corrected to 60% of the energy N60. Thus, according to the shear wave velocity profile of the study site,

N_{60} was estimated using the expressions and parameters shown in Tables 2 and 3, obtaining N_{60}=27, for the first

210 10 m of depth.

Table 2 Correlations to estimate shear wave velocity.

Reference	Correlation	N_{60}
(Pitilakis et al., 1999)	$V_s = 145 N_{60}^{0.178}$	$N_{60} = (V_s/145)^{(1/0.178)}$
(Dikmen, 2009)	$V_s = 73 N^{0.33}$	$N = (V_s/73)^{(1/0.33)}$
(Imai, 1977)	$V_s = 80.6 N^{0.331}$	$N = (V_s/80.6)^{(1/0.331)}$

Note: N: SPT blow counts, N_{60}: blow counts 60% energy corrected.

Table 3 Parameters for estimating N60.

Depth from (m)	to (m)	(Pitilakis et al., 1999) N_{60}	(Dikmen, 2009) N	N_{60}	(Imai, 1977) N	N_{60}
0	10	25	45	32	33	24
10	20	214	145	103	106	75
20	30	65	76	54	56	40

215

The safety factor against liquefaction for the embankment SF_l, was calculated based on the critical strength ratio

CSR, which was derived from the site response analysis. A correction factor for the magnitude of the earthquake

was applied. The CRR was obtained using the (Robertson and Wride, 1998) approximation, and the magnitude

correction factor, MSF, proposed by (Andrus and Stokoe, 1999): was considered through the following

220 equations

$$CRR_{7.5} = \frac{1}{34-(N_1)_{60}} + \frac{(N_1)_{60}}{135} + \frac{50}{[10*(N_1)_{60}+45]^2} - \frac{1}{200} \tag{1}$$

$$MSF = \left(\frac{M_w}{7.5}\right)^{-2.56} \tag{2}$$

$$SF_l = \left(CRR_{7.5}/CSR\right) MSF \qquad (3)$$

The preliminary result shows that in the first 10 m of the profile there is the potential for soil liquefaction.

225 **Table 4 Safety factor against liquefaction**

Average depth (m)	CSR	CRR_{7.5}	MSF	SF_l
1	0.66	0.34	0.85	0.44
3	0.64	0.34	0.85	0.45
5	0.62	0.34	0.85	0.46
7	0.59	0.34	0.85	0.49
9	0.53	0.34	0.85	0.54
11	0.46	Not liquefiable	0.85	>1.0
13	0.43	Not liquefiable	0.85	>1.0
15	0.42	Not liquefiable	0.85	>1.0
17	0.40	Not liquefiable	0.85	>1.0
19	0.37	Not liquefiable	0.85	>1.0
21	0.34	Not liquefiable	0.85	>1.0
23	0.31	Not liquefiable	0.85	>1.0
25	0.28	Not liquefiable	0.85	>1.0
27	0.26	Not liquefiable	0.85	>1.0
29	0.25	Not liquefiable	0.85	>1.0

Note: *CSR*: critical strength ratio, *CRR_{7.5}*: cyclical resistance ratio, *MSF*: magnitude correction factor, and *SF_l*: safety factor against liquefaction.

The seismic response of the embankment was evaluated using a three-dimensional finite difference model, Figure 15, considering a depth of 110 m in the soil profile, as well as the parameters of site S4. Tables 5 and 6

230 show the soil profile and the embankment characteristics, respectively.
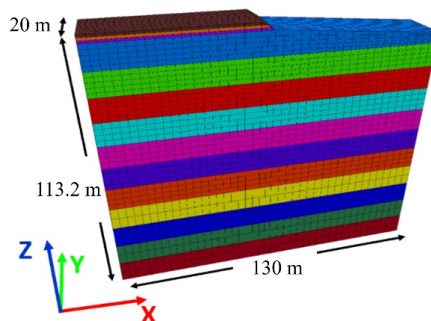
Figure 15: Soil profile and road embankment in the three-dimensional finite difference model. Each colour represents soil layers according to depths indicated in Table 5.

Table 5 Soil characteristics.

Depth (m)	Density (kg/m³)	Poisson ratio	C (kNm²)	φ (°)	V_s (m/s)	E (kN/m²)	G (kN/m²)	K (kN/m²)
0-10	1.7	0.3	4.9	30	257	291,937	112,283	243,280
10-20	1.7	0.3	4.9	35	377	628,210	241,619	523,508
20-30	1.7	0.3	4.9	35	305	411,170	158,142	342,642
30-40	1.7	0.3	4.9	35	332	487,190	187,381	405,992
40-50	1.7	0.3	4.9	35	424	794,610	305,619	662,175

Height	Density	Poisson	C	φ	Vs	E	G	K
50-60	1.7	0.3	4.9	35	510	1,149,642	442,170	958,035
60-70	1.7	0.3	4.9	35	572	1,446,153	556,213	1,205,128
70-80	1.7	0.3	4.9	38	610	1,644,682	632,570	1,370,568
80-90	1.7	0.3	4.9	38	628	1,743,177	670,453	1,452,648
90-100	1.7	0.3	4.9	38	656	1,902085	731,571	1,585,071
100-110	1.7	0.3	4.9	38	646	1,844,537	709,437	1,537,114

235   Note: C: soil shear strength, φ: friction angle, V_s: shear wave velocity, E: Young's modulus, G: shear stiffness, K: constraint modulus.

Table 6 Embankment characteristics.

Height (m)	Density (kg/m³)	Poisson ratio	C (kN/m²)	φ (°)	Vs (m/s)	E (kN/m²)	G (kN/m²)	K (kN/m²)
0-1.3	1.4	0.35	4.9	30	285	307,968	114,062	342,187
1.3-2.6	1.4	0.35	4.9	30	264	263,334	97,531	292,593
2.6-4.0	1.4	0.35	4.9	30	241	218,700	81,000	243,000

Note: C: soil shear strength, φ: friction angle, V_s: shear wave velocity, E: Young's modulus, G: shear stiffness, K: constraint modulus.

240   For calibration purposes, one-dimensional models were developed with the program FLAC3d, to solve the equation of motion in the time domain, considering both equivalent linear and non-linear properties, and the results were compared with those obtained in the frequency domain, with the program SHAKE (Fig. 16). The sig3 model available in FLAC was used to approximately represent soil non-linearity. Thus, the sig3 hysteretic model was used to address the variation of the stiffness modulus and the damping ratio during the seismic event.

245   This model considers an ideal soil, in which the stress depends only on the deformation, and not on the number of cycles loads. With these assumptions an incremental constitutive relationship of the degradation curve can be described by $\tau n / \gamma = G / G_{max}$, where τn is the normalized shear stress, γ is the shear strain, and G/G_{max} is the normalized secant modulus. The sig3 model is defined using the following expression:

$$\frac{G}{G_{max}} = \frac{a}{1+\exp\left(-\frac{L-x_0}{b}\right)} \tag{4}$$

250   where L is the logarithmic deformation, defined as $L = log10\ (\gamma)$, and the parameters a, b and x_0, used by the sig3 model, were obtained through an iterative process, in which the modulus degradation curves were fitted with the model. The corresponding damping is given directly by the hysteresis loop during cyclic loading. For the case study, the parameters a, b and x_0 take the values 1.014, −0.50 and −1.25, respectively. Figure 16 shows a comparison between the curves used in the deterministic unidimensional model (Seed and Idriss, 1970), and

255   those obtained with the sig3 model. Figure 17 shows a comparison between the response spectra calculated on the surface with the deterministic one-dimensional model, the equivalent linear FLAC3D, and the non-linear FLAC3D. Good agreement between the results was observed.

(a) (b)
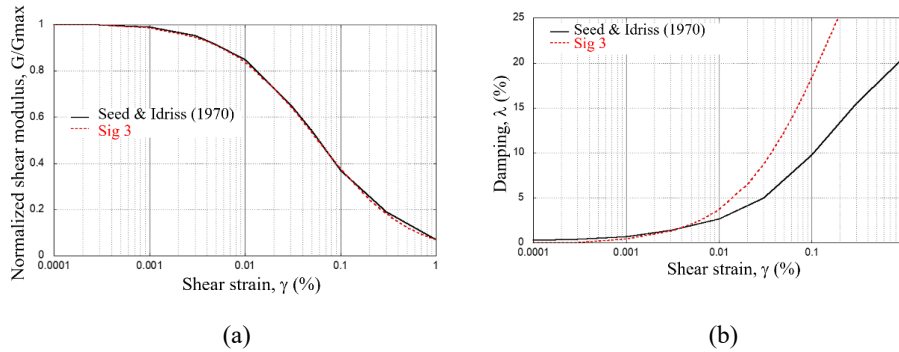
Figure 16: Results obtained from (Seed and Idriss, 1970) and sig3 model.
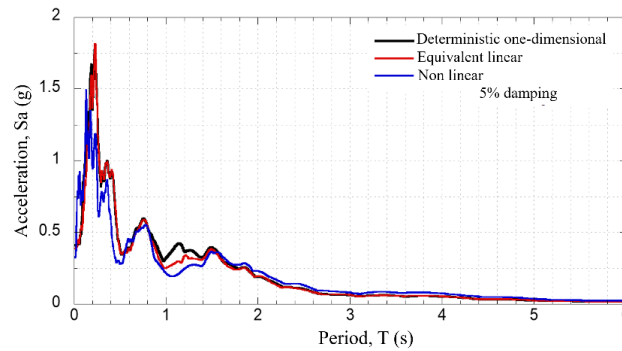
260 **Figure 17: Response spectra at the surface with the different types of analyses.**

For the three-dimensional model, the Finn-Byrne model was used to evaluate the liquefaction potential. This model is defined as:

$$(\Delta\epsilon_{vd})_{\frac{1}{2}ciclo} = C_1 \exp\left(-C_2\left(\frac{\epsilon_{vd}}{\gamma}\right)\right) \qquad (5)$$

where $\Delta\epsilon vd$ is the decrease in volume per half cycle of deformation; γ is the shear strain, and $C1$ and $C2$ are

265 constants that can be calculated as:

$$C_1 = \frac{1}{2}C_1^c; \ C_2 = \frac{0.4}{C_1^c}; C_1^c = 87 \ (N_1)_{60}^{-1.25} \qquad (6)$$

These parameters, presented in Table 7, were calculated using the average values of $(N_1)_{60}$, for the first 10 m of soil and the embankment.

Table 7 Coefficients used for the Finn-Byrne model

Element	C_1^c	C_1	C_2
Soil (0 a 10 m)	0.14	0.07	2.82
Embankment (0 to 1.3 m)	0.08	0.04	4.71
Embankment (1.3 to 2.6 m)	0.12	0.06	3.21
Embankment (2.6 to 4.0 m)	0.19	0.10	2.07

270

Five scenarios were considered to assess the seismic performance of the road embankment, considering the variations in sea level registered in the study area, as well as the case of high tide, and soil saturation due to rain, Table 8 and Figure 18.

275   **Table 8 Sea level for each evaluated scenario.**

Scenario	Tide	Sea level
1	Low tide	0.00 m
2	Average sea level	0.38 m
3	High tide	0.68 m
4	Maximum tide	1.28 m
5	Maximum tide and storm	1.28 m

Seven control points were established in the model to obtain the soil behaviour parameters. Control points were located along the fault surface, at the toe of the embankment, at the highest point of the embankment, and within the soil deposit, Figure 18. Using the concept of static safety factor, SF_s, prior the application of the seismic

280   loading, the general stability of the embankment under static conditions was evaluated for each scenario. SF_s was above 2 in all the scenarios considered. The static safety factor was computed based on the concept of the strength over demand concept.
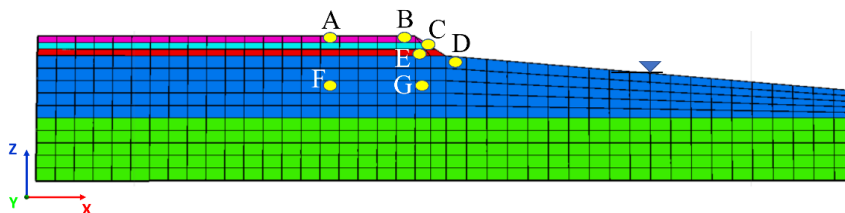
Figure 18: Model monitoring points.

285   Next, an analysis of the seismic response was performed applying the N90E acceleration history, Figure 11. It was observed that the largest vertical displacement, = 73 cm, was recorded in scenario 5, on the crest of the embankment. Figure 19 presents the results of vertical displacement for scenarios 4 and 5 at the end of the earthquake. Figure 20 gives the results of the horizontal displacement for the same cases. The largest horizontal displacement was observed in scenario 5, = 51 cm. Important vertical displacements of the soil were observed,

290   as well as a tendency of lateral displacement of the body of the slope, increasing with depth.

At the control points, Figure 21 shows the pore pressure ratio, r_u, obtained for each scenario. A rise in pore pressure was observed at points G and F, in all scenarios. However, with the increase of the sea level, the higher pore pressure ratio at point D, located at the toe of the slope, continues to increase in scenarios 3 and 4, and reaches values above 0.7 in scenario 5, where an additional increase in this ratio was observed at point E, located

295   on the failure surface of the slope.
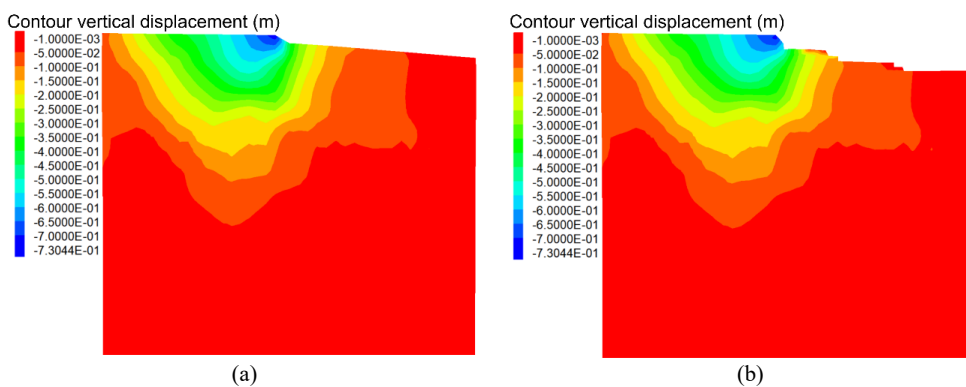
Figure 19: Permanent vertical displacements for scenarios (a) 4 and (b) 5.
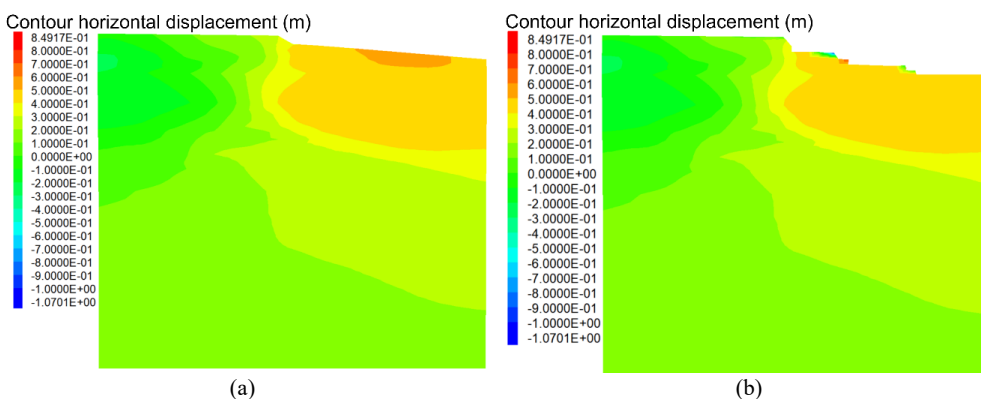
Figure 20: Permanent horizontal displacements for scenarios (a) 4 and (b) 5.

(c)   (d)

(e)
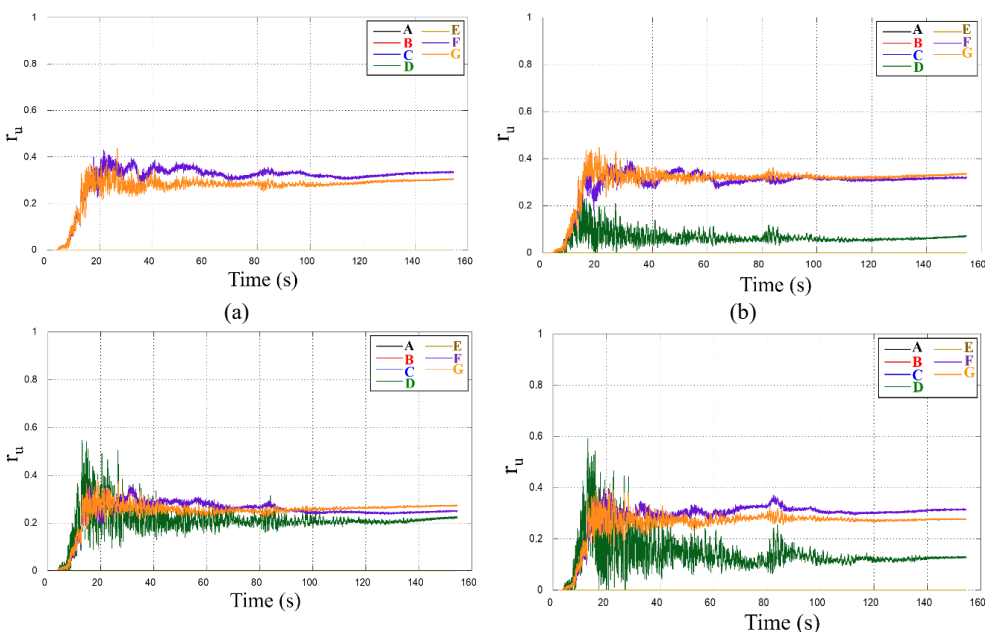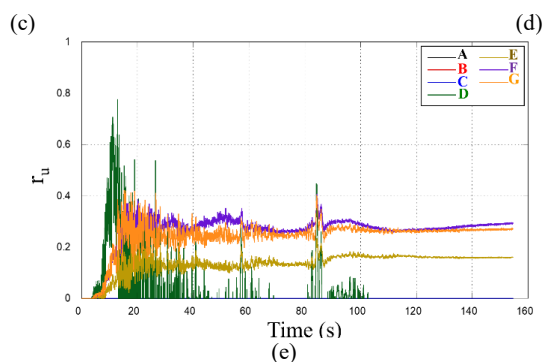
Figure 21: Variations of pore pressure ratios in scenarios (a) 1, (b) 2, (c) 3, (d) 4 and (e) 5.

3.4.   Step 2: simulation of tsunami and wave propagation

300   The tsunami simulation was carried out using the model implemented in the GeoClaw code (Berger et al., 2011), which is based on solving the non-linear shallow water equations through the numerical method of finite volumes. The bathymetric and topographic information used was obtained from the GEBCO database generated by the NOAA, with a resolution of 15 arc seconds. Considering the characteristics of the fault mechanism of the 1995 Manzanillo earthquake, Table 9, the (Okada, 1995) fault model was used to estimate the vertical

305   displacement on the seabed caused by the seismic event.

Table 9 Fault characteristics of the 1995 Manzanillo earthquake

Event	Strike	Length (km)	Width (km)	Depth (km)	Slip	Rake	Dip	Longitude (°	Latitude (°)
09/10/1995	309	200 e^3	107 e^3	10 e^3	1.35	104	14	-104	19

Based on the calculated deformations and the characteristics of the earthquake, a tsunami-wave propagation model was run for a simulation period of 1 hour, beginning 15 minutes after the start of the earthquake. Figure

310   22 shows the simulation results for time 1 min.
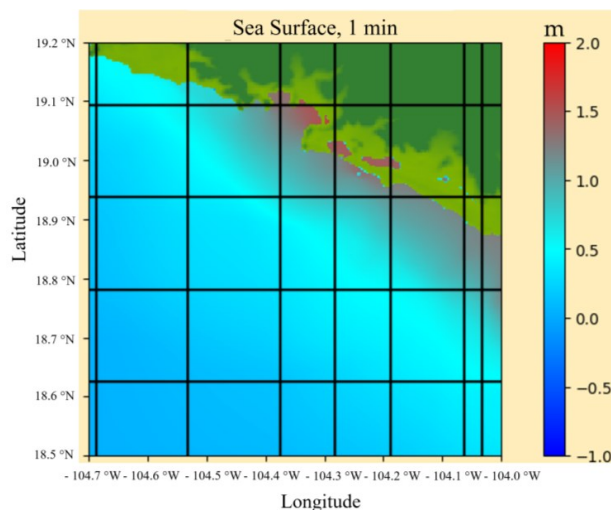
Figure 22: Sea surface elevation obtained after a simulation time of 1 minute.

Wave speeds and elevations were obtained at 5 virtual gauges in Santiago Bay, near the road embankment studied. These are shown in Table 10 and Figure 23. Figure 24 shows the change in bathymetry at the gauge locations, as well as the free sea surface elevation, respectively. Figure 25 shows the free sea surface elevation, and u and v the wave velocity components at the gauge nearest to the coast, as well as the wave speed s.

Table 10 Location of virtual gauges in the simulation

Gauge	Longitude (°W)	Latitude (°N)
Gauge 1	-104.38	19.07
Gauge 2	-104.38	19.08
Gauge 3	-104.38	19.09
Gauge 4	-104.38	19.10
Gauge 5	-104.38	19.11

Figure 23: Location of gauges used to obtain the free sea surface elevations and speeds in the simulation. (© Google Earth).

(a)

Wave height (m)

(b)
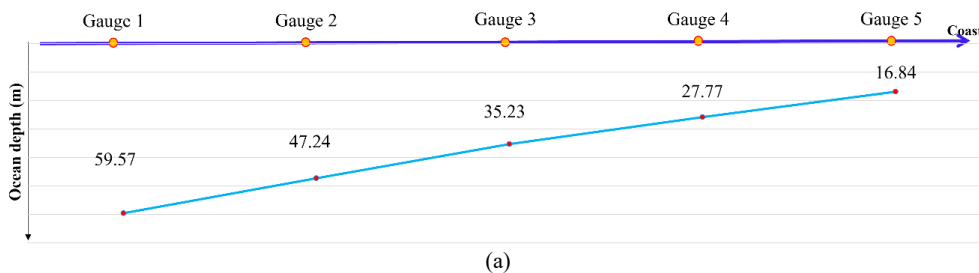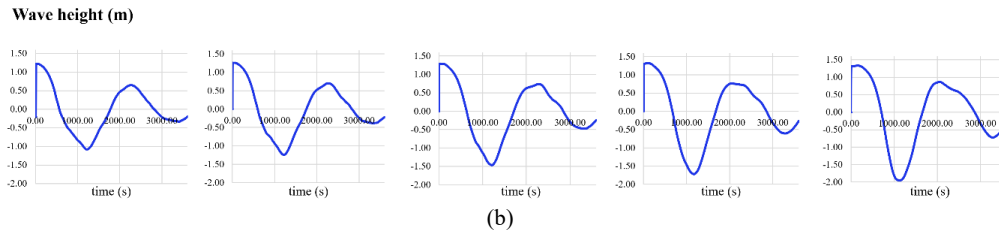
Figure 24: (a) Ocean depths at the gauge locations (top) and (b) wave height distribution obtained during the simulation (bottom).
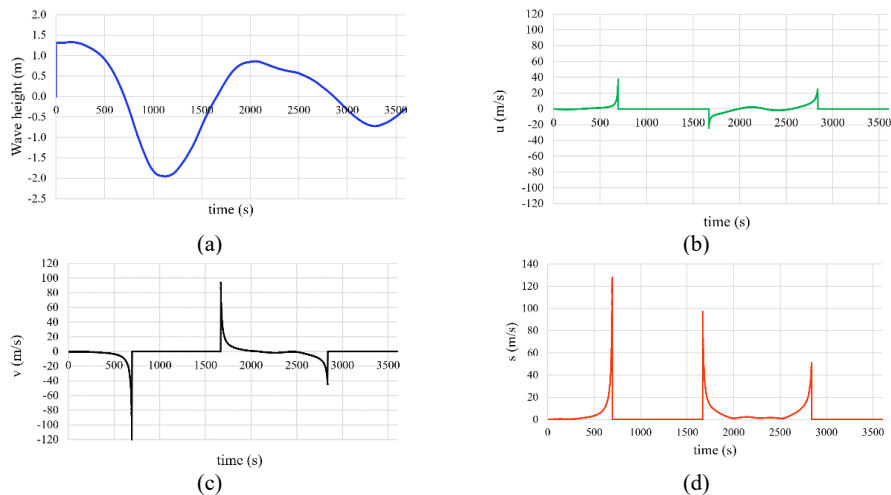
Note: *u*: horizontal velocity, *v*: vertical velocity, *s*: wave speed.

325 **Figure 25: For the gauge nearest to the coast: (a) free sea surface elevation (b) velocity *u*, (c) velocity *v*, and (d) wave speed *s*.**

It is worth mentioning that the maximum flood levels obtained coincide with the visual data reported by Avila et al., (2005).

3.5. Step 3: earthquake-tsunami response

330 Applying a smooth particle hydrodynamics approach, the wave-induced hydrodynamic pressures associated with tsunami flooding at the study site were determined from the speeds and free sea surface elevation from Gauge 5. The hydrodynamic pressures were obtained using the speeds and free sea surface elevations of this gauge, the closest to the coast, Figure 24, using the SPH DualSPHysics model. This model has been widely used for hydrodynamic forces and to model complex fluid flows (González-Cao et al., 2019; Ye et al., 2019).

335 Figure 26 shows the pressures acting on the road embankment and Figure 27 shows the pressure evolution at points a, b, c, d, e and f, obtained in the first 90 s of loading, corresponding to the wave colliding with the slope of the embankment. The parameters and main characteristics of the simulations are shown in Table 11. The occupied Kernel function is the Wendland function, the time-step algorithm used is Symplectic, the viscosity scheme used is the artificial viscosity ($\alpha = 0.01$) and the inter-particle spacing was 0.1 m. The simulations were

340 run on NVIDIA 1650 GPU.

Table 11 Parameters and main characteristics of the SPH simulation

Parameters	Value
Kernel Function	Wendland
Time-step	Algorithm Symplectic
Viscosity Artificial	$\alpha=0.01$
Inter-particle spacing (m)	0.1
Number of particles	104,825
Simulated time (s)	90
Time out (s)	0.1
Computing time (h)	9.18
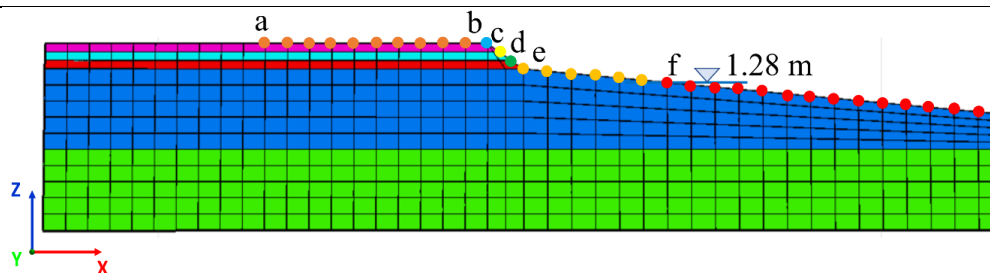
Figure 26: Initial sea level and control points considered for the earthquake-tsunami loading analysis.
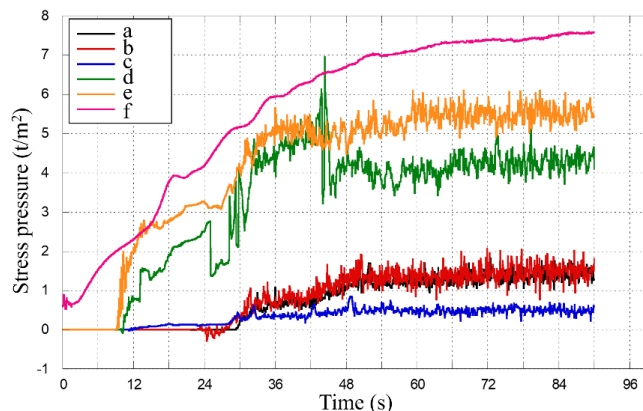
Figure 27: Loading variation stress as a function of time at points a-f.

The wave-induced behaviour at the embankment was analysed, applying the same time-step numerical approach of Step 1, and the conditions of Scenario 5, with an initial maximum tide of 1.28 m and saturated soil. From the results obtained in Steps 1 and 2, the corresponding wave elevation of 1.5 m was modelled. In the model, the hydrodynamic pressures, pore pressures and incremental hydrostatic vertical loading were applied until the steady state in each of the loading points was reached.

Figure 28 shows the hydrostatic and hydrodynamic loading conditions applied at 50 s. The resulting vertical and horizontal displacements, and the safety factor (i.e. capacity over demand) obtained from steady state loading conditions are shown in Figures 29 to 31.
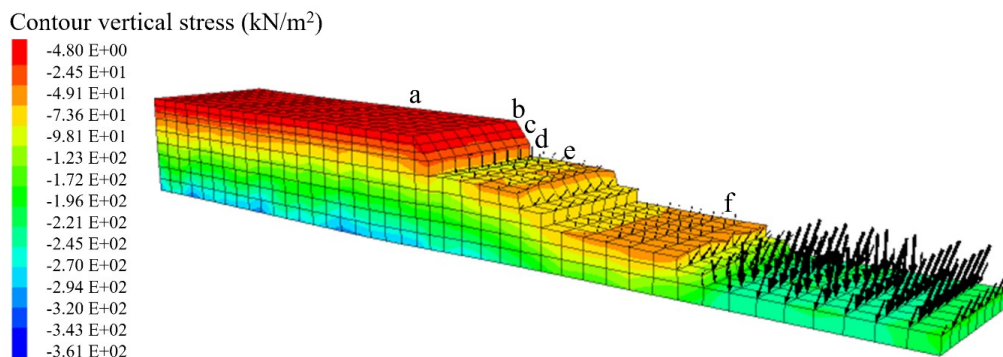
355   **Figure 28: Loading conditions at points a, b, c, d, e and f, at time 50 s.**

| (a) | (b) |
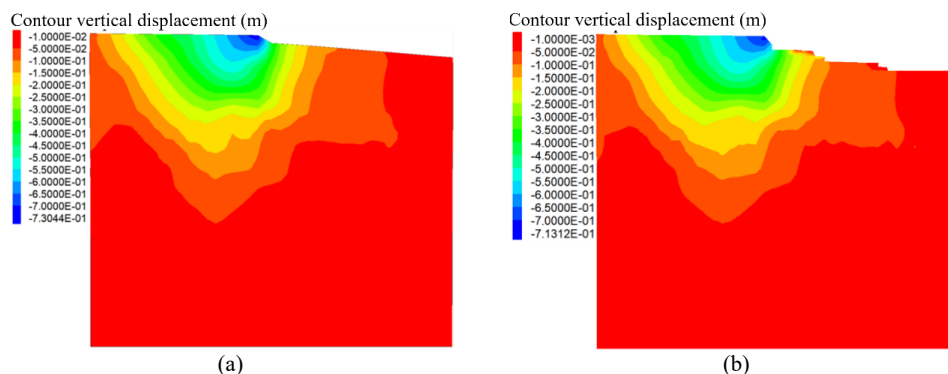
Figure 29: Vertical displacements contours in meters (a) after seismic loading, (b) after tsunami loading.

| (a) | (b) |
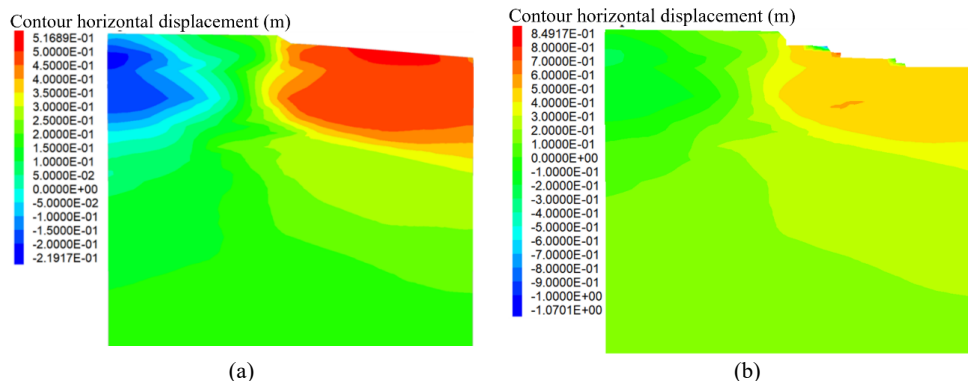
Figure 30: Horizontal displacement contours in meters (a) after seismic loading, (b) after tsunami loading.

(a)   (b)
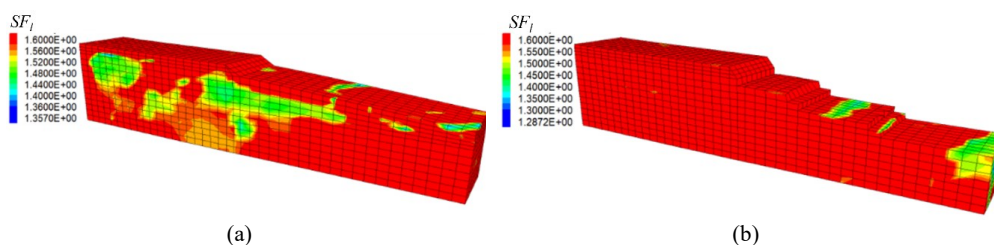
Figure 31: Safety factor versus liquefaction (a) after seismic loading, (b) after tsunami loading.

360   The analysis shows that the main effects induced by wave loading are the horizontal displacement of the beach slope, reaching 0.8 m near to point f. No major impacts were seen in the road embankment, where both vertical and horizontal displacements and the liquefaction safety factor show minor variations. However, there was a loss of granular material due to excessive ground deformation in the beach area. This effect was simulated following a time step approach, where zones of the mesh that reach a deformation of 2 m were removed from

365   the model. The hydrodynamic loads were applied to the remaining mesh, which allowed the incremental unloading of the unstable areas in the sand found on the beach slope. The coupled effect of liquefaction and a tsunami could potentially lead to a loss of functionality of the road associated with an approximate 0.7m displacement of the slope.

370   **4.   Conclusions**

A sequential methodology was implemented to analyse the response of transportation infrastructure in an earthquake-tsunami. The methodology was applied for Manzanillo, Mexico, where the behaviour of a section of a road embankment was analysed, considering the accumulated effects of the earthquake in terms of horizontal and vertical displacements, and those induced by an increase in sea level after the earthquake. In the

375   case study, different scenarios were analysed depending on the initial elevation of the sea. The seismic response of the embankment showed that the most critical condition occurred in the scenarios of maximum high tide, and maximum high tide with saturated soil. In these scenarios the vertical displacements were 0.57 m and 0.73 m, respectively, both of which occurred at the embankment crest. The vertical and horizontal displacements can be interpreted as a failure of the embankment, in the sense that they may imply loss of functionality, since these

380   gives a 20% reduction in the height of the structure.

The simulation of wave propagation of a tsunami showed that the level of the free sea surface could increase 1.5 m in the Manzanillo Bay area (Avila-Armella et al., 2005). Further analysis of the earthquake-tsunami behaviour showed that for the scenario of maximum high tide and saturated soil, the highest variation in the horizontal displacements in the ground between the stage at the end of the earthquake and the stage at the end

385   of tsunami-induced flooding, is seen on the beach slope. In the case study, the sequential model shows that seismic loading causes the greatest effects in pore pressure increase and in ground failure due to vertical and horizontal displacements in the embankment.

From this study it is clear that, as in other parts of the world, the road network in Manzanillo has been built to improve communications, but ignoring many coastal processes, such as the potential presence of a tsunami.

390 Moreover, this infrastructure, was built on coastal dune ridges, inducing coastal squeeze, isolating ecosystems and increasing risk. The planning, design and construction of infrastructure in coastal areas susceptible to earthquakes and tsunamis should be rethought in order to make it compatible with natural processes and thus truly contribute to a better quality of life (Chávez et al., 2021; Silva et al., 2021). In the case of Manzanillo, a pile-driven road is probably a better option.

395 **References**

Akiyama, M., Frangopol, D. M., and Ishibashi, H.: Toward life-cycle reliability-, risk- and resilience-based design and assessment of bridges and bridge networks under independent and interacting hazards: emphasis on earthquake, tsunami and corrosion, Structure and Infrastructure Engineering, 16, 26-50, 10.1080/15732479.2019.1604770, 2020.

Altomare, C., Crespo, A. J. C., Domínguez, J. M., Gómez-Gesteira, M., Suzuki, T., and Verwaest, T.: Applicability of Smoothed Particle Hydrodynamics for estimation of sea wave impact on coastal structures, Coastal Engineering, 96, 1-12, https://doi.org/10.1016/j.coastaleng.2014.11.001, 2015.

Andrus, R. D. and Stokoe, K. H.: Liquefaction resistance based on shear wave velocity, NCEER Workshop on Evaluation of Liquefaction Resistance of Soils, Salt Lake City, UT, Technical Report NCEER-97-0022, T. L. Youd and I. M. Idriss, eds., National Center for Earthquake Engineering Research, Buffalo, NY, 89–128., 1999.

Argyroudis, S. and Kaynia, A. M.: Analytical seismic fragility functions for highway and railway embankments and cuts, Earthquake Engineering & Structural Dynamics, 44, 1863-1879, https://doi.org/10.1002/eqe.2563, 2015.

Argyroudis, S. A. and Mitoulis, S. A.: Vulnerability of bridges to individual and multiple hazards- floods and earthquakes, Reliability Engineering & System Safety, 210, 107564, https://doi.org/10.1016/j.ress.2021.107564, 2021.

Attary, N., Van De Lindt, J. W., Barbosa, A. R., Cox, D. T., and Unnikrishnan, V. U.: Performance-Based Tsunami Engineering for Risk Assessment of Structures Subjected to Multi-Hazards: Tsunami following Earthquake, Journal of Earthquake Engineering, 25, 2065-2084, 10.1080/13632469.2019.1616335, 2021.

Avila-Armella, A., Pedrozo-Acuna, A., Silva-Casarin, R., and Simmonds, D.: Prediction of tsunami-induced flood on the Mexican Pacific coast, Ingenieria Hidraulica en Mexico, 20, 5-18, 2005.

Berger, M. J., George, D. L., LeVeque, R. J., and Mandli, K. T.: The GeoClaw software for depth-averaged flows with adaptive refinement, Advances in Water Resources, 34, 1195-1206, https://doi.org/10.1016/j.advwatres.2011.02.016, 2011.

Bhattacharya, S., Hyodo, M., Nikitas, G., Ismail, B., Suzuki, H., Lombardi, D., Egami, S., Watanabe, G., and Goda, K.: Geotechnical and infrastructural damage due to the 2016 Kumamoto earthquake sequence, Soil Dynamics and Earthquake Engineering, 104, 390-394, 10.1016/j.soildyn.2017.11.009, 2017.

Briaud, J.-L. and Maddah, L.: Minimizing roadway embankment damage from flooding, Project 20-05 (Topic 46-16), Transportation Research Board, Washington, D.C.2016.

Burns Patrick, O., Barbosa Andre, R., Olsen Michael, J., and Wang, H.: Multihazard Damage and Loss Assessment of Bridges in a Highway Network Subjected to Earthquake and Tsunami Hazards, Natural Hazards Review, 22, 05021002, 10.1061/(ASCE)NH.1527-6996.0000429, 2021.

Cervantes, O., Verduzco-Zapata, G., Botero, C., Olivos-Ortiz, A., Chávez-Comparan, J. C., and Galicia-Pérez, M.: Determination of risk to users by the spatial and temporal variation of rip currents on the beach of Santiago Bay, Manzanillo, Mexico: Beach hazards and safety strategy as tool for coastal zone management, Ocean & Coastal Management, 118, 205-214, https://doi.org/10.1016/j.ocecoaman.2015.07.009, 2015.

Chávez, V., Lithgow, D., Losada, M., and Silva-Casarin, R.: Coastal green infrastructure to mitigate coastal squeeze, Journal of Infrastructure Preservation and Resilience, 2, 7, 10.1186/s43065-021-00026-1, 2021.

Chinnarasri, C., Thanasisathit, N., Ruangrassamee, A., Weesakul, S., and Lukkunaprasit, P.: The impact of tsunami-induced bores on buildings, Proceedings of the Institution of Civil Engineers - Maritime Engineering, 166, 14-24, 10.1680/maen.2010.31, 2013.

440   Cubrinovski, M.: Liquefaction-Induced Damage in the 2010-2011 Christchurch (New Zealand) Earthquakes, International Conference on Case Histories in Geotechnical Engineering, 1-11,

DeMets, C. and Wilson, D. S.: Relative motions of the Pacific, Rivera, North American, and Cocos plates since 0.78 Ma, Journal of Geophysical Research: Solid Earth, 102, 2789-2806, https://doi.org/10.1029/96JB03170, 1997.

Dikmen, Ü.: Statistical correlations of shear wave velocity and penetration resistance for soils, Journal of
445   Geophysics and Engineering, 6, 61-72, 10.1088/1742-2132/6/1/007, 2009.

Dizhur, D., Giaretton, M., and Ingham, J. M.: Damage Observations Following the Mw 7.8 2016 Kaikoura Earthquake, Proceedings of the International Conference on Earthquake Engineering and Structural Dynamics, Cham, 249-261,

EQE International: "The October 9, 1995 Manzanillo, Mexico earthquake: Summary of structural damage", A
450   summary report, EQE International, 6 - 14, 1996.

Escudero Castillo, M., Mendoza Baldwin, E., Silva Casarin, R., Posada Vanegas, G., and Arganis Juaréz, M.: Characterization of Risks in Coastal Zones: A Review, CLEAN – Soil, Air, Water, 40, 894-905, https://doi.org/10.1002/clen.201100679, 2012.

González-Cao, J., Altomare, C., Crespo, A. J. C., Domínguez, J. M., Gómez-Gesteira, M., and Kisacik, D.: On
455   the accuracy of DualSPHysics to assess violent collisions with coastal structures, Computers & Fluids, 179, 604-612, https://doi.org/10.1016/j.compfluid.2018.11.021, 2019.

Iai, S.: Evaluation of performance of port structures during earthquakes, Soil Dynamics and Earthquake Engineering, 2019.

Imai, T.: P and S wave velocities of the ground in Japan, Proc. 9th ICSMFE, 257-260,
460   Ishibashi, H., Akiyama, M., Frangopol, D. M., Koshimura, S., Kojima, T., and Nanami, K.: Framework for estimating the risk and resilience of road networks with bridges and embankments under both seismic and tsunami hazards, Structure and Infrastructure Engineering, 17, 494-514, 10.1080/15732479.2020.1843503, 2021.

Jose, J., Choi, S.-J., Giljarhus, K. E. T., and Gudmestad, O. T.: A comparison of numerical simulations of
465   breaking wave forces on a monopile structure using two different numerical models based on finite difference and finite volume methods, Ocean Engineering, 137, 78-88, https://doi.org/10.1016/j.oceaneng.2017.03.045, 2017.

Kakderi, K. and Pitilakis, K.: Fragility Functions of Harbor Elements, in: SYNER-G: Typology Definition and Fragility Functions for Physical Elements at Seismic Risk: Buildings, Lifelines, Transportation Networks and
470   Critical Facilities, edited by: Pitilakis, K., Crowley, H., and Kaynia, A. M., Springer Netherlands, Dordrecht, 327-356, 10.1007/978-94-007-7872-6_11, 2014.

Karafagka, S., Fotopoulou, S., and Pitilakis, K.: Analytical tsunami fragility curves for seaport RC buildings and steel light frame warehouses, Soil Dynamics and Earthquake Engineering, 2018.

Klapp, J., Areu-Rangel, O. S., Cruchaga, M., Aránguiz, R., Bonasia, R., Godoy, M. J., and Silva-Casarín, R.:
475   Tsunami hydrodynamic force on a building using a SPH real-scale numerical simulation, Natural Hazards, 100, 89-109, 10.1007/s11069-019-03800-3, 2020.

Koshimura, S., Hayashi, S., and Gokon, H.: The impact of the 2011 Tohoku earthquake tsunami disaster and implications to the reconstruction, Soils and Foundations, 54, 560-572, https://doi.org/10.1016/j.sandf.2014.06.002, 2014.

480   Kramer, S. L.: Geotechnical earthquake engineering, Pearson Education India1996.

Maruyama, Y., Yamazaki, F., Mizuno, K., Tsuchiya, Y., and Yogai, H.: Fragility curves for expressway embankments based on damage datasets after recent earthquakes in Japan, Soil Dynamics and Earthquake Engineering, 30, 1158-1167, https://doi.org/10.1016/j.soildyn.2010.04.024, 2010.

Mayoral, J. M., Argyroudis, S., and Castañon, E.: Vulnerability of floating tunnel shafts for increasing
485   earthquake loading, Soil Dynamics and Earthquake Engineering, 80, 1-10, https://doi.org/10.1016/j.soildyn.2015.10.002, 2016.

Mayoral, J. M., Badillo, A., and Alcaraz, M.: Vulnerability and recovery time evaluation of an enhanced urban overpass foundation, Soil Dynamics and Earthquake Engineering, 100, 1-15, https://doi.org/10.1016/j.soildyn.2017.05.023, 2017.

490   McKenna, G., Argyroudis, S. A., Winter, M. G., and Mitoulis, S. A.: Multiple hazard fragility analysis for granular highway embankments: Moisture ingress and scour, Transportation Geotechnics, 26, 100431, https://doi.org/10.1016/j.trgeo.2020.100431, 2021.

NIBS: Users's manual and technical manuals. In Report Prepared for the Federal Emergency Management Agency; National Institute of Building Sciences: Washington, DC, USA, 2004.

495   Okada, M.: Tsunami observation by ocean bottom pressure gauge, in: Tsunami: progress in prediction, disaster prevention and warning, Springer, 287-303, 1995.

Ovando-Shelley, E. and Romo, M.: Three Recent Damaging Earthquakes in Mexico, International Conference on Case Histories in Geotechnical Engineering2004.

Pitilakis, K., Raptakis, D., Lontzetidis, K., Tika-Vassilikou, T., and Jongmans, D.: Geotechnical and
500   geophysical description of EURO-SEISTEST, using field, laboratory tests and moderate strong motion recordings, Journal of Earthquake Engineering, 3, 381-409, 1999.

Robertson, P. K. and Wride, C.: Evaluating cyclic liquefaction potential using the cone penetration test, Canadian Geotechnical Journal, 35, 442-459, 10.1139/t98-017, 1998.

Rowell, M. and Goodchild, A.: Effect of Tsunami Damage on Passenger and Forestry Transportation in Pacific
505   County, Washington, Transportation Research Record, 2604, 88-94, 10.3141/2604-11, 2017.

Sarkis, A., Palermo, A., Kammouh, O., and Cimellaro, G.: Seismic resilience of road bridges: lessons learned from the 14 November 2016 Kaikōura Earthquake, Proceedings of the 9th International Conference on Bridge Maintenance, Safety, Melbourne, Australia, 9-13,

Seed, H., Idriss, I., Makdisi, F., and Banerjee, N.: Representation of irregular stress time histories by equivalent
510   uniform stress series in liquefaction analyses. EERC 75-29, Earthquake Engineering Research Center, University of California, Berkeley, 1975.

Seed, H. B. and Idriss, I. M.: Analyses of ground motions at Union Bay, Seattle during earthquakes and distant nuclear blasts, Bulletin of the Seismological Society of America, 60, 125-136, 10.1785/BSSA0600010125, 1970.

515   Silva, R., Martínez, M. L., van Tussenbroek, B. I., Guzmán-Rodríguez, L. O., Mendoza, E., and López-Portillo, J.: A Framework to Manage Coastal Squeeze, Sustainability, 12, 10610, 2020.

Silva, R., Oumeraci, H., Martínez, M. L., Chávez, V., Lithgow, D., van Tussenbroek, B. I., van Rijswick, H. F. M. W., and Bouma, T. J.: Ten Commandments for Sustainable, Safe, and W/Healthy Sandy Coasts Facing Global Change, Frontiers in Marine Science, 8, 10.3389/fmars.2021.616321, 2021.

520   Silva, R., Chávez, V., Bouma, T. J., van Tussenbroek, B. I., Arkema, K. K., Martínez, M. L., Oumeraci, H., Heymans, J. J., Osorio, A. F., Mendoza, E., Mancuso, M., Asmus, M., and Pereira, P.: The Incorporation of Biophysical and Social Components in Coastal Management, Estuaries and Coasts, 42, 1695-1708, 10.1007/s12237-019-00559-5, 2019.

Tonatiuh Dominguez, R., Rodríguez-Lozoya, H. E., Sandoval, M. C., Sanchez, E. S., Meléndez, A. A.,
525   Rodríguez- Leyva, H. E., and Amelia Campos, R.: Site response in a representative region of Manzanillo, Colima, Mexico, and a comparison between spectra from real records and spectra from normative, Soil Dynamics and Earthquake Engineering, 93, 113-120, https://doi.org/10.1016/j.soildyn.2016.11.013, 2017.

Williams, J. H., Wilson, T. M., Horspool, N., Paulik, R., Wotherspoon, L., Lane, E. M., and Hughes, M. W.: Assessing transportation vulnerability to tsunamis: utilising post-event field data from the 2011 Tōhoku
530   tsunami, Japan, and the 2015 Illapel tsunami, Chile, Nat. Hazards Earth Syst. Sci., 20, 451-470, 10.5194/nhess-20-451-2020, 2020.

Ye, T., Pan, D., Huang, C., and Liu, M.: Smoothed particle hydrodynamics (SPH) for complex fluid flows: Recent developments in methodology and applications, Physics of Fluids, 31, 011301, 10.1063/1.5068697, 2019.

535